Influence of dual conduit structure on solute transport in karst tracer tests: An experimental laboratory study

Chaoqi Wang, Xiaoguang Wang, Samer Majdalani, Vincent Guinot, Hervé Jourde

This is the preprint of a paper published in Journal of Hydrology Volume 590, November 2020, 125255, https://doi.org/10.1016/j.jhydrol.2020.125255

Influence of dual conduit structure on solute transport in karst tracer tests: an experimental laboratory study

Chaoqi Wang[1], Xiaoguang Wang[1], Samer Majdalani[1], Vincent Guinot[1], Herve Jourde[1]

1. Hydrosciences Montpellier, UMR 5569, France

Abstract

We conducted lab-scale experiments to investigate the mechanism of dual-peaked breakthrough curves (BTCs) in karst tracer tests. Three groups of dual conduit structures were constructed by varying: (1) the length ratio between the two conduits for a fixed length of the shorter conduit, (2) the total length of the conduits for a fixed length ratio, (3) the connection angle between the conduits. The BTCs generated by the tracing experiments were fitted by a Dual-Region Advection Dispersion (DRAD) model to derive effective transport parameters.

Our results confirm that the dual conduit structure triggers the double-peaked BTCs. Increasing the conduit length for a fixed length ratio or increasing the length ratio increases peak separation. The connection angles between the two conduits θ_1 and θ_2 also influence the BTCs: increasing θ_1 and decreasing θ_2 causes the first peak to get smaller and the second peak to get larger. The DRAD model can reproduce the dual-peaked BTCs while its application to the case of single-peaked BTCs may be problematic due to strong interaction between model parameters. A method is proposed for estimating underground karstic conduit lengths from experimental dual-peaked BTCs.

Keywords: karst conduit; tracer test, laboratory experiment; breakthrough curve; MCMC

This is the preprint of a paper published in Journal of Hydrology Volume 590, November 2020, 125255, https://doi.org/10.1016/j.jhydrol.2020.125255

Highlights:

1. The effect of dual conduit structure on solute transport is investigated using lab experiments
2. Increasing length ratio or total conduit length cause larger separation of dual peaks of BTCs
3. The connection angle affects tracer partition to the two conduits
4. A method for estimating the length of subsurface karst conduits based on BTCs is proposed

This is the preprint of a paper published in Journal of Hydrology Volume 590, November 2020, 125255, https://doi.org/10.1016/j.jhydrol.2020.125255

1. Introduction

The methodology of tracer test initially developed for the investigation of karst aquifers is still widely used in karst hydrogeology. Tracer tests can provide information about groundwater trajectories and yield breakthrough curves (BTCs) that can be used to estimate transport model parameters (Goldscheider and Drew, 2007).

Due to the strong heterogeneity of karst aquifers, the BTCs may exhibit asymmetry with long tails or multiple peaks (Moreno and Tsang, 1991; Hauns et al., 2001; Massei et al., 2006; Perrin and Luetscher, 2008, Goldscheider et al., 2008). The Advection–Dispersion-Equation (ADE) performs poorly in characterizing these BTCs. To better reproduce tailing effects, some researchers considered including further processes in the transport model (Morales et al., 2010): the Mobile-Immobile Model (MIM) developed by van Genuchten and Wierenga (1976) partitions the aquifer into mobile and immobile regions; Skopp et al. (1981) proposed a dual-permeability model (also referred to as the Multiple Region Advection-Dispersion (MRAD) by Majdalani et al. (2018)) with two mobile regions using the ADE model. Berkowitz et al. (2006) proposed the Continuous Time Random Walk (CTRW) theory by conceptualizing solute transport as a series of particle jumps or transitions with spatially changing velocities, recently CTRW was also applied to karst aquifers (Goeppert et al., 2020). Dual-peaked BTCs were successfully modeled by the application of the Dual Advection Dispersion Equation (DADE) and the Weighted Sum Advection-Dispersion Equation (WSADE) model (Field and Leij, 2012).

Dual-peaked BTCs in karst tracer tests may be caused by the presence of pools (or underground lakes) along main conduits (Field and Leij, 2012; Dewaide, 2018) or multiple flow paths (Maloszewski et al., 1992; Goldscheider et al., 2008; Perrin and Luetscher, 2008). This hypothesis has been investigated using laboratory scale experiments in the past (Moreno and Tsang, 1991; Field and Leij, 2012). Among the different experiments used for a better understanding of karst aquifer solute transport, some scale models account for both the conduit and the matrix (Florea and Wicks, 2001; Li et al., 2008; Mohammadi et al., 2019), while others focus on transport in conduits only (Zhao et

al., 2017, 2019; Field and Leij, 2012). Field and Leij (2012) noted that the presence of pools or auxiliary conduits causes dual-peaked BTCs. Mohammadi et al. (2019) studied how the hydraulic head gradient influences BTCs by a bench-scale karst model. Zhao et al. (2017, 2019) found that the existence of pools on the conduit would increase the tailing of BTCs. However, these studies did not show whether karst conduit properties can be inferred from BTC shapes.

To better assess the relationship between conduit structure and BTCs, we studied how the dual conduit geometry influences the BTCs shape by laboratory tracer experiments. Three groups of solute transport experiments were carried out. The obtained BTCs were fitted using a one-dimensional transport model to achieve a quantitative comparison.

2 Materials and methods

2.1 Experimental setup

A series of lab-scale, idealized dual conduit structure models were built using silicone pipes with an internal diameter of 0.4 cm. The dual conduit structure consists of three parts: the inlet, dual conduit and outlet. At the inlet and outlet parts, the flow is restricted in the single conduit; at the dual conduit part, the flow is divided into two conduits of different lengths (Fig. 1). The shorter and the longer conduit lengths are denoted as l_1 and l_2, respectively. The deviation angles between the shorter and longer conduits at both the inlet and outlet connecting part are denoted respectively as θ_1 and θ_2. During the experiments, the dual conduit structure is placed on a horizontal platform to eliminate gravity effects.

This is the preprint of a paper published in Journal of Hydrology Volume 590, November 2020, 125255,
https://doi.org/10.1016/j.jhydrol.2020.125255

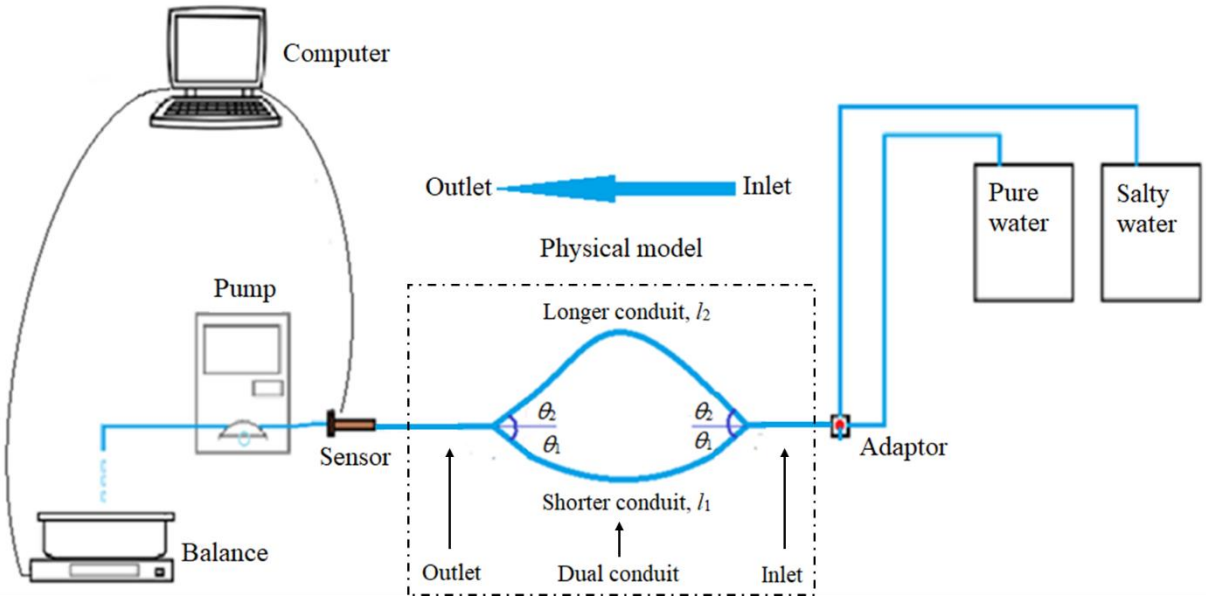

Figure 1. Schematic diagram showing the experimental setup used in the study.

The inflowing flow is supplied using a peristaltic pump (Lead Fluid brand) at a constant rate. The discharge Q is set at 0.6846 cm^3/s, and hence the calculated velocity through the outlet conduit is 5.4480 cm/s. The inlet is connected in parallel to a pure water supply and a salty water supply. A three-way adapter is used to switch between the salty water and pure water. The salty water (deionized water + NaCl at $C_0 = 0.06$ mol/L) is used as the tracer. A pulse tracer release is realized by switching the adaptor to the salty water supply for 5 seconds (3.42 mL). The physical models were fully sealed and the recovery rate was 100% for all of the experiments.

We use a scale (Mettler Toledo™) to estimate the discharge. A conductimeter (WTW TetraCon 325™, accuracy is 1×10^{-6} mol/L), is used to measure the outlet tracer concentration. The scale and conductimeter are connected to a data logger (Campbell CR1000™) for automatic data recording at a time step of 1 second (In order to obtain more accurate peak time, the BTCs have been interpolated by 0.05 s.). In each experiment, the tracer injection is initiated after the flow within the system is stabilized. Each experiment is repeated three times. A mean BTC is derived from the replicates to reduce the measurement error.

This is the preprint of a paper published in Journal of Hydrology Volume 590, November 2020, 125255,
https://doi.org/10.1016/j.jhydrol.2020.125255

Three groups of experiments are performed (Table 1). The notation for the experiment name takes the format of l_1 - l_2 - θ_1 - θ_2 (Fig. 1). Experiment Group 1 is designed to study the effect of length ratio of the two conduits on the transport process. l_1 is set at 10 cm, while l_2 is set to 20 cm, 40 cm, 60 cm, and 120 cm, respectively. The angles θ_1 and θ_2 are both fixed at 30 degrees. Experiment Group 2 is designed to study the effect of total conduit length variation on the transport process, keeping the length ratio of two conduits as 1:6. l_1 is set to be 10 cm, 20 cm and 60 cm and l_2 is set to be 60 cm, 120 cm, and 360 cm, respectively. The angles θ_1 and θ_2 of the connectors are also fixed at 30 degrees. Experiment Group 3 is designed to study the effect of the conduit connection angle on the transport process. l_1 is set at 10 cm and l_2 is 60 cm, and three different connection types are made by arranging the θ_1 and θ_2 combinations. In total, eight tracer tests are presented (the 10-60-30-30 experiment is used in all of the three groups as a reference case).

Table 1. Geometrical parameters of dual conduit structures for the three groups of experiments

Group	Experiment label	Conduit length (cm)		Connection angles (deg)	
		l_1	l_2	θ_1	θ_2
1	10-20-30-30	10	20	30	30
	10-40-30-30	10	40	30	30
	10-60-30-30	10	60	30	30
	10-120-30-30	10	120	30	30
2	10-60-30-30	10	60	30	30
	20-120-30-30	20	120	30	30
	60-360-30-30	60	360	30	30
3	10-60-30-120	10	60	30	120
	10-60-30-30	10	60	30	30
	10-60-120-30	10	60	120	30

This is the preprint of a paper published in Journal of Hydrology Volume 590, November 2020, 125255,
https://doi.org/10.1016/j.jhydrol.2020.125255

2.2 One-dimensional modeling

2.2.1 Dual Region Advection Dispersion (DRAD) model

To quantitatively investigate the dual-peaked BTCs obtained in section 2.1, we apply a Dual Region Advection Dispersion (DRAD) model. This model has been called Two-Region MRAD model by Majdalani et al. (2018) and DADE model by Field and Leij (2012). DRAD model assumes two regions flowing in parallel and exchanging mass due to concentration difference; in both regions, the ADE model is assumed valid (Fig. 2). We do not consider solute degradation or adsorption/desorption in our model. The DRAD model is chosen because it is the possible simplest model to reproduce the dual-peaked BTCs.

The governing equations are given as follows:

$$\frac{\partial C_i}{\partial t} + u_i \frac{\partial C_i}{\partial x} - D_i \frac{\partial^2 C_i}{\partial x^2} = \frac{k_{ij}}{w_i}(C_j - C_i), (i = 1, 2; j = 2, 1), \quad (1)$$

$$k_{12} = k_{21}, \quad (2)$$

$$w_1 + w_2 = 1. \quad (3)$$

The total concentration at the outlet is computed as:

$$C(x,t) = w_1 C_1(x,t) + w_2 C_2(x,t), \quad (4)$$

where t is time (T), x is distance (L), C_i is the concentration (ML^{-3}) of region i, u_i, D_i and w_i are respectively the flow velocity (LT^{-1}), dispersion coefficient (L^2T^{-1}) and volumetric fraction in region i, k_{ij} is the coefficient for solute exchange between regions i and j (T^{-1}). Since we consider only two-region systems, $k_{12} = k_{21}$, and $w_1 + w_2 = 1$. As a result, six independent parameters are involved in the calibration: w_1, k_{12}, u_1, u_2, D_1 and D_2. In our discussions, the fast and slow regions are denoted by region 1and region 2 respectively (i.e., $u_1 > u_2$).

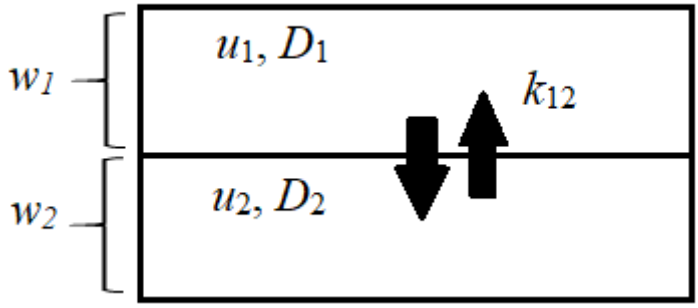

Figure 2. Schematic diagram of the DRAD model.

2.2.2 DRAD model parameter estimation

The six independent DRAD model parameters were estimated using the MCMC method (Haario et al., 2006). The MCMC method is a Bayesian approach that evaluates the posterior distributions of parameters for an assumed error structure (Vrugt et al., 2006). Using the Bayes rule, the probability density function of the model parameter set $\boldsymbol{\theta}=\{w_1, k_{12}, u_1, u_2, D_1, D_2\}$ is given as:

$$p(\boldsymbol{\theta}|\mathbf{Y}) \propto L(\boldsymbol{\theta}|\mathbf{Y}) \cdot p(\boldsymbol{\theta}), \tag{5}$$

where $p(\boldsymbol{\theta})$ and $p(\boldsymbol{\theta}|\mathbf{Y})$ are the prior and posterior parameter distribution, respectively, $Y = \{y(t_1), \dots, y(t_n)\}$ is the observations, $L(\boldsymbol{\theta}|\mathbf{Y})$ is the likelihood function. The prior distribution $p(\boldsymbol{\theta})$ is assumed to follow a uniform distribution. The model residual for outlet concentrations are assumed to be independent and follow a Gaussian distribution with zero mean and a constant variance σ^2. Thus, the posterior distribution is given by:

$$p(\boldsymbol{\theta}|\mathbf{Y}, \sigma^2) \propto \frac{1}{(2\pi\sigma^2)^{N/2}} \exp\left(-\frac{\sum_i^n (C_i - Y_i)^2}{2\sigma^2}\right), \tag{6}$$

where N is the number of observations, C_i and Y_i are the simulated and observed concentrations time i. The convergence performance of MCMC chains is evaluated with a Root-Mean-Square-Error (RMSE) objective function, which is defined as:

$$RMSE = \sqrt{\frac{\sum_{i=1}^n (C_i - Y_i)^2}{N}}. \tag{7}$$

We used the Metropolis-Hastings (MH) algorithm to successively draw samples from the posterior distribution by forming a Markov chain of model parameter set $\boldsymbol{\theta}$. The MH algorithm constructs a Markov chain in four main steps: (1) choose an initial parameter set $\boldsymbol{\theta}^0$ and a proposal density distribution $q(\boldsymbol{\theta}_k|\boldsymbol{\theta}_{k-1})$; (2) at each iteration k + 1, generate a new sample $\boldsymbol{\theta}^*$ from $q(\boldsymbol{\theta}^*|\boldsymbol{\theta}^k)$ and calculate the probability of acceptance, $\pi = \min\left(\frac{p(\boldsymbol{\theta}^*)L(\boldsymbol{\theta}^*|\mathbf{Y})q(\boldsymbol{\theta}^k|\boldsymbol{\theta}^*)}{p(\boldsymbol{\theta}_k)L(\boldsymbol{\theta}_k|\mathbf{Y})q(\boldsymbol{\theta}^*|\boldsymbol{\theta}^k)}, 1\right)$, draw a random number u from a uniform distribution between 0 and 1; (3) if $\pi > u$, set $\boldsymbol{\theta}^{k+1} = \boldsymbol{\theta}^*$; otherwise $\boldsymbol{\theta}^{k+1} = \boldsymbol{\theta}^k$; (4) repeat steps 2 and 3 until a given maximum number of iteration is reached. To achieve a fast convergence of the chain, we first perform a manual fitting of the DRAD response to the experimental BTCs to find the initial parameter set. In this work, we assume the posterior distribution is Gaussian. For each chain, 16000 iterations are executed, and the last 1000 sampled parameter sets that allow the model to adequately fit the observed data were chosen to evaluate the posterior parameter distribution and the pairwise parameter correlations. Except for 10-20-30-30, all of the fitted parameters are set to be the mean value of these 1000 sets. For 10-20-30-30, the fitted parameters are chosen with the criterion: $w_1 > 0.5$.

The parameter correlations are characterized by scatterplots of parameter pairs and the correlation coefficient r, which is a statistical measure of the linear relationship between two variables. Given paired data $\{(x_1, y_1), (x_2, y_2), \ldots, (x_n, y_n)\}$, r is defined as:

$$r = \frac{\sum_{i=1}^{n}\left(x_i - \bar{x}\right)\left(y_i - \bar{y}\right)}{\sqrt{\sum_{i=1}^{n}\left(x_i - \bar{x}\right)^2}\sqrt{\sum_{i=1}^{n}\left(y_i - \bar{y}\right)^2}}, \tag{8}$$

where n is the sample size; $\bar{x}$ and $\bar{y}$ are the mean value for x and y, respectively. The parameter variability (or uncertainty) is represented by the parameter histogram and relative standard deviation (RSD) value. RSD is calculated by:

$$\mathrm{RSD} = \frac{\sqrt{\frac{\sum_{i=1}^{n}\left(x_i - \bar{x}\right)^2}{n-1}}}{\left|\bar{x}\right|}. \tag{9}$$

This is the preprint of a paper published in Journal of Hydrology Volume 590, November 2020, 125255,
https://doi.org/10.1016/j.jhydrol.2020.125255

3. Results

3.1 Length ratio study (experiment Group 1)

The BTCs from Experiment Group 1 (Fig. 3) trigger the following observations. When the length ratio is small (e.g., 2), the BTC only exhibits a single peak; for length ratio of 4, 6 and 12, the BTCs exhibit two peaks. As the length ratio increases, the first peak arrives slightly earlier while the arrival of the second peak is delayed. The value of the first peak (C_{peak1}) decreases first from the 10-20-30-30 to the 10-40-30-30 case and then increases as the length ratio is further increased. The concentration value of the second peak (C_{peak2}) decreases as the length ratio increases.

Using the DRAD model and the MCMC calibration algorithm, we try to correctly fit the experimental BTCs. Visually the simulated BTCs can capture the main shape of the experimental BTCs. The overall fitting performance is quite good for the 10-40-30-30 system with a maximum error value of 0.0233 (Table 2). However, the recession limb of the second peak of some experimental BTCs (Fig. 3b, c) exhibits a slight skewness, which the DRAD model is unable to capture exactly (Fig. 3b, c, d). For the first experiment (Fig. 3a), the DRAD model allows a good fit for the BTC curve. For the dual-peaked BTCs (Fig. 3b, c), the fit of the second peak is not as good as the fit of the first peak but the overall BTC behavior is correctly reproduced by the DRAD model. The parameters of the fitting result for Group 1 are listed in Table 2 and plotted in Figure 4. We do not plot the variation of the exchange rate k_{12} because of the very small values that indicate a negligible exchange rate and therefore a negligible effect on the BTC.

This is the preprint of a paper published in Journal of Hydrology Volume 590, November 2020, 125255,
https://doi.org/10.1016/j.jhydrol.2020.125255

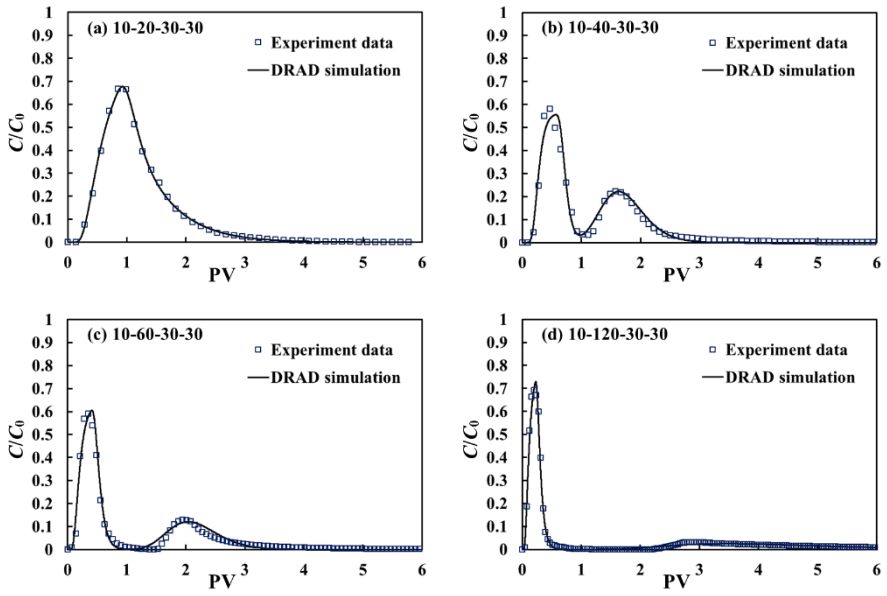

160

161 **Figure 3.** DRAD calibration results of Group 1 experiments.

162 **Table 2.** DRAD model calibration results for Group 1 experiments

	10-20-30-30	**10-40-30-30**	**10-60-30-30**	**10-120-30-30**
t_{peak1} (s)	6.45	4.85	4.55	4.40
t_{peak2} (s)	6.45	17.20	27.85	73.00
u_1 (m/s)	4.46×10^{-2}	5.04×10^{-2}	5.13×10^{-2}	5.09×10^{-2}
u_2 (m/s)	1.89×10^{-2}	9.40×10^{-3}	5.27×10^{-3}	1.46×10^{-3}
u_1 (m/PV)	3.17×10^{-1}	5.43×10^{-1}	7.41×10^{-1}	1.29×10^{0}
u_2 (m/PV)	1.34×10^{-1}	1.01×10^{-1}	7.61×10^{-2}	3.71×10^{-2}
D_1 (m^2/s)	5.71×10^{-4}	3.99×10^{-4}	7.42×10^{-4}	1.05×10^{-3}
D_2 (m^2/s)	3.86×10^{-4}	4.03×10^{-5}	1.82×10^{-5}	1.47×10^{-5}
k_{12} (1/s)	7.14×10^{-37}	3.25×10^{-25}	3.08×10^{-28}	1.99×10^{-26}
w_1 (–)	0.526	0.562	0.632	0.653
RMSE (–)	0.00967	0.0233	0.0165	0.0120

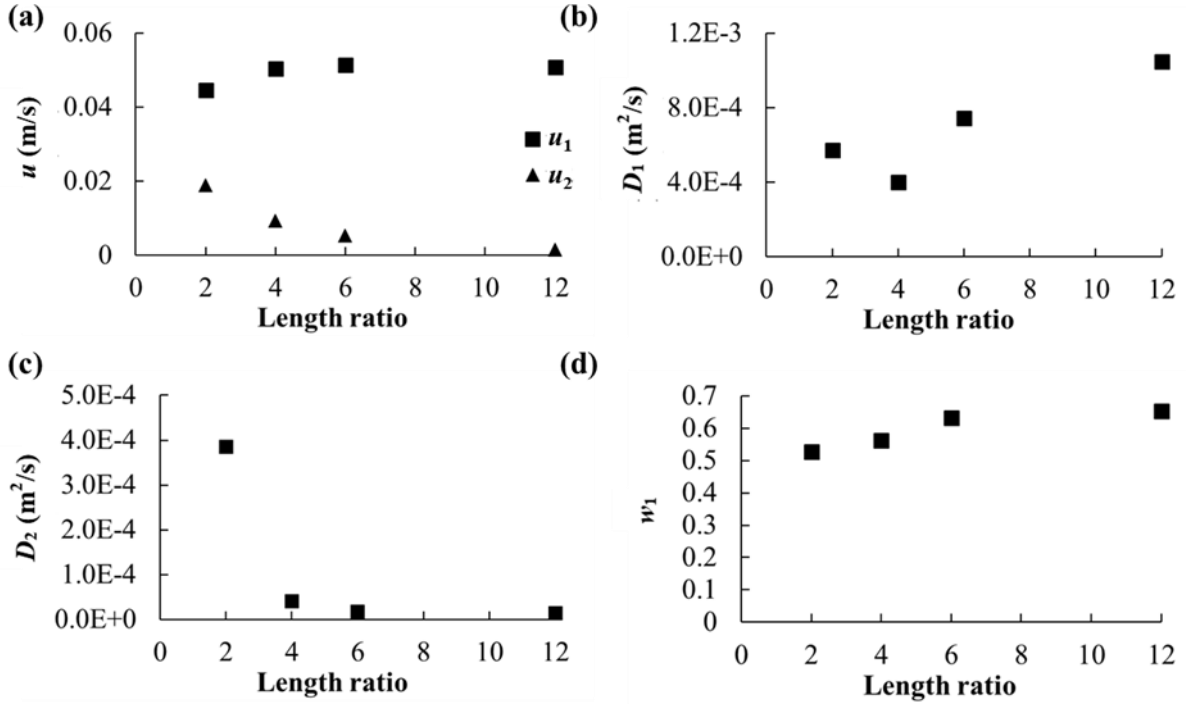

Figure 4. Variation of fitted parameter values with experimental model length for Group 1 experiments. (a) Velocities in the two regions, u_1 and u_2, (b) Dispersion coefficient of region 1, D_1, (c) Dispersion coefficient of region 2, D_2, (d) Water content ratio of region 1, w_1.

From Figure 4a, we find that, as the length ratio increases from 2 to 12, the velocity of region 1 (u_1) increases from 4.46×10^{-2} to 5.09×10^{-2} (1:1.14). The major increase in u_1 value occurs when transiting between 10-20-30-30 and 10-40-30-30 cases, while the u_1 is only slightly increased from 10-40-30-30 to 10-120-30-30 cases. The velocity of region 2 (u_2) shows a significant decreasing trend, decreases from 1.89×10^{-2} to 1.46×10^{-3} (12.9:1) from 10-20-30-30 to 10-120-30-30 and u_2 decreases from 9.40×10^{-3} to 1.46×10^{-3} (6.45:1) from 10-40-30-30 to 10-120-30-30. This is consistent with the fact that from 10-40-30-30 to 10-120-30-30 the second peak gets increasingly delayed (Fig. 3). As we can see from Figure 4b, the D_1 value does not show any continuous increasing trend: as the ratio increases from 2 to 12, D_1 increases from 5.71×10^{-4} to 1.05×10^{-3} (1:1.84), and as the ratio increases from 4 to 12, D_1 increases from 3.99×10^{-4} to 1.05×10^{-3} (1:2.63). Such behavior of D_1 variation may be caused by the strong correlation between

some parameters for the case of 10-20-30-30 (see parameter identifiability results in Section 3.4 and discussion in Section 4.3). As the ratio increases from 2 to 12, D_2 decreases from 3.86×10^{-4} to 1.47×10^{-5} (2.73:1). As the ratio increases from 2 to 12, w_1 increases from 0.526 to 0.653 (1:1.24), w_2 decreases from 0.474 to 0.347 (1.36:1). This is in agreement with the trend observed from Figure 3 (except for the experiment 10-20-30-30, which only has one peak): as the length ratio increases, the area below the second peak (A_2), and, thus, the mass transported through the longer conduit decreases.

3.2 Total length study (experiment Group 2)

In this series of experiments, the length ratio is fixed to 6.0 and the total length (l_1+l_2) varies. The experimental BTCs and the numerical fitting of Group 2 are shown in Figure 5. For Group 2, all of the tested dual conduit structures exhibit double-peaked BTCs. As the length increases, the two peaks become increasingly separated. As the length increases, both C_{peak1} and C_{peak2} show a decreasing trend, with C_{peak2} decreasing faster than C_{peak1}. For the experiment 60-360-30-30, the longer conduit has a strong flow resistance. Thus, the amount of tracer that enters this conduit is much less. As a result, the second peak has a very low concentration value (0.0148) and is hardly visible on the plot.

A visual inspection indicates that the DRAD does not equally capture the two peaks of the experimental BTCs. Similar to the analysis of Group 1 results, the skewness of the second peak in the BTCs is not perfectly reproduced by the DRAD model. The parameters of the fitting result are listed in Table 3. The fitted parameters for Group 2, except the exchange rate k_{12} that remains negligible, are plotted in Figure 6.

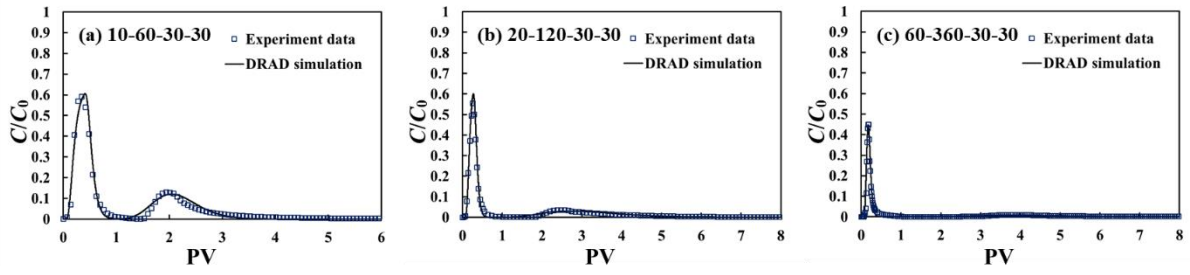

This is the preprint of a paper published in Journal of Hydrology Volume 590, November 2020, 125255,
https://doi.org/10.1016/j.jhydrol.2020.125255

194 **Figure 5.** DRAD calibration results for Group 2 experiments.

195 **Table 3.** DRAD model calibration results for Group 2 experiments

	10-60-30-30	**20-120-30-30**	**60-360-30-30**
t_{peak1} (s)	4.55	7.20	16.30
t_{peak2} (s)	27.85	5.90	291.60
u_1 (m/s)	5.13×10^{-2}	5.18×10^{-2}	5.25×10^{-2}
u_2 (m/s)	5.27×10^{-3}	2.99×10^{-3}	2.03×10^{-3}
u_1 (m/PV)	7.41×10^{-1}	1.41×10^{0}	4.13×10^{0}
u_2 (m/PV)	7.61×10^{-2}	8.16×10^{-2}	1.60×10^{-1}
D_1 (m^2/s)	7.42×10^{-4}	1.11×10^{-3}	1.63×10^{-3}
D_2 (m^2/s)	1.82×10^{-5}	4.43×10^{-5}	4.77×10^{-5}
k_{12} (1/s)	3.08×10^{-28}	4.01×10^{-52}	1.56×10^{-38}
w_1 (–)	0.633	0.635	0.721
RMSE (–)	0.0165	0.00620	0.00895

196

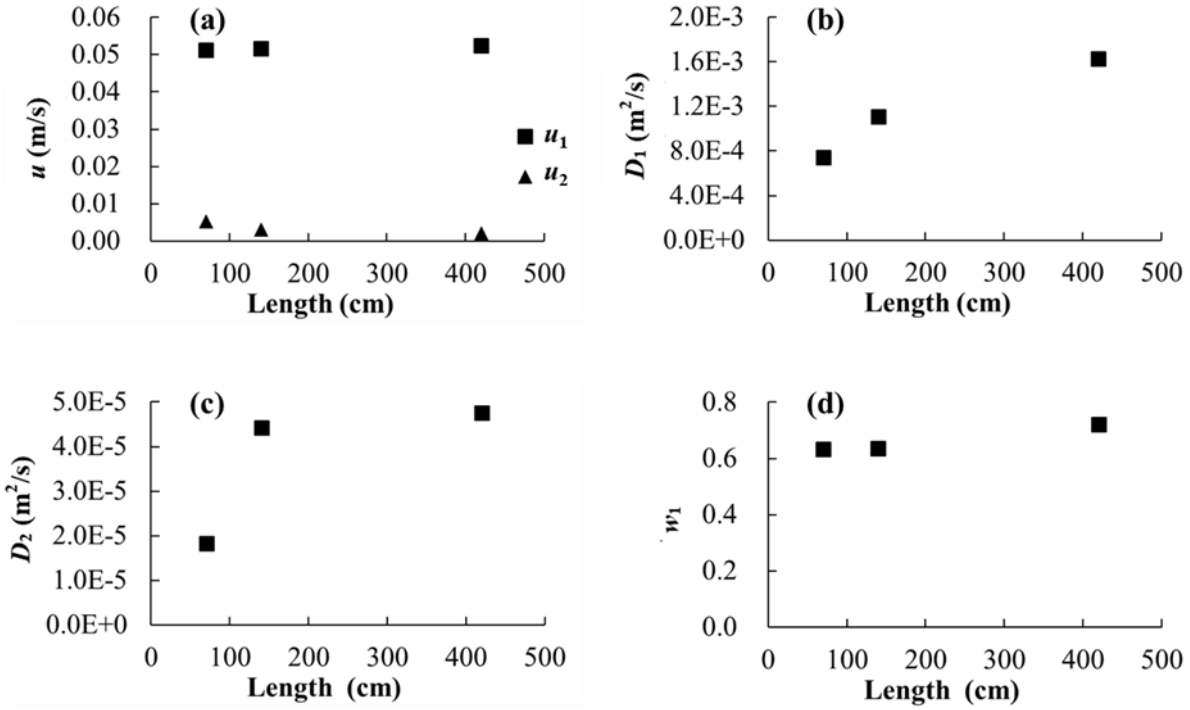

Figure 6. Variation of fitted parameter values with experimental model length for Group 2 experiments. (a) Velocities in the two regions, u_1 and u_2, (b) Dispersion coefficient of region 1, D_1, (c) Dispersion coefficient of region 2, D_2, (d) Water content ratio of region 1, w_1.

As shown in Figure 6. As the length increases from 10cm-60cm to 60cm-360cm (1:6), the velocity u_1 increases from 5.13×10^{-2} to 5.25×10^{-2} (1:1.02), and u_2 decreases from 5.27×10^{-3} to 2.03×10^{-3} (2.60:1) (Fig. 6a). The dispersion coefficient of both regions increases: D_1 increases from 7.42×10^{-4} to 1.63×10^{-3} (1:2.19), D_2 increases from 1.82×10^{-5} to 4.77×10^{-5} (1:2.62), (Fig. 6 b, c). w_1 remains almost the same, from 0.633 to 0.721 (1:1.14), (Fig. 6d).

3.3 Connection angle (experiment Group 3)

For Group 3 experiments (Fig. 7), the connector angle between two conduits has an important influence on the flow and transport process. As the (θ_1-θ_2) value increases, the two peaks become closer to each other; C_{peak1} decreases, C_{peak2} increases.

This is the preprint of a paper published in Journal of Hydrology Volume 590, November 2020, 125255,
https://doi.org/10.1016/j.jhydrol.2020.125255

Same with previous groups, the fit is better for the first peak of the experiment BTCs than for the second peak, with a maximum error value to be 0.0168 (Table 4). The fitted parameters for Group 3 are plotted in Figure 8.

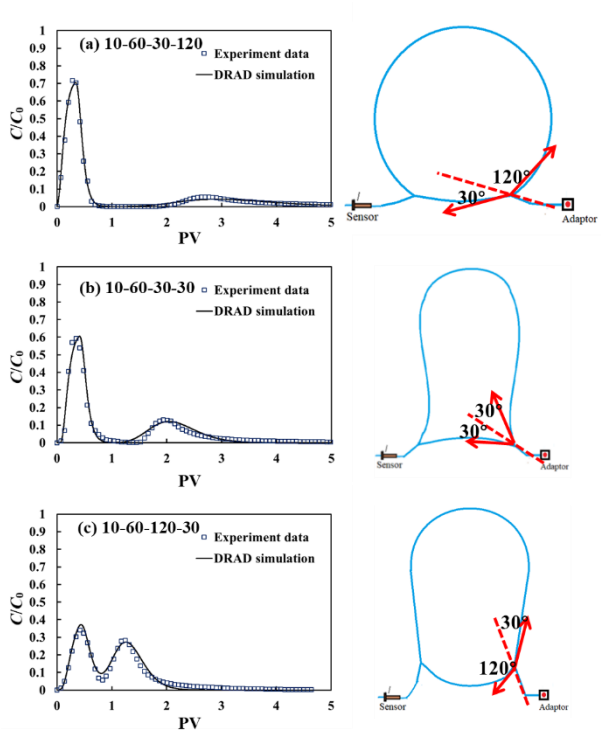

Figure 7. DRAD calibration results of Group 3 experiments.

Table 4. DRAD model calibration results for Group 3 experiments

	10-60-30-120	**10-60-30-30**	**10-60-120-30**
$(\theta_1-\theta_2)$ (deg)	-90	0	90
t_{peak1} (s)	4.40	4.55	6.15
t_{peak2} (s)	39.65	27.85	17.60
u_1 (m/s)	5.39×10^{-2}	5.13×10^{-2}	2.99×10^{-2}
u_2 (m/s)	3.31×10^{-3}	5.27×10^{-3}	8.56×10^{-3}
u_1 (m/PV)	7.78×10^{-1}	7.41×10^{-1}	4.32×10^{-1}
u_2 (m/PV)	4.78×10^{-2}	7.61×10^{-2}	1.24×10^{-1}
D_1 (m^2/s)	7.81×10^{-4}	7.42×10^{-4}	3.55×10^{-4}
D_2 (m^2/s)	2.22×10^{-5}	1.82×10^{-5}	3.17×10^{-5}
k_{12} (1/s)	6.33×10^{-34}	2.19×10^{-33}	9.28×10^{-26}
w_1 (-)	0.732	0.633	0.451

RMSE (-)	0.0131	0.0165	0.0168

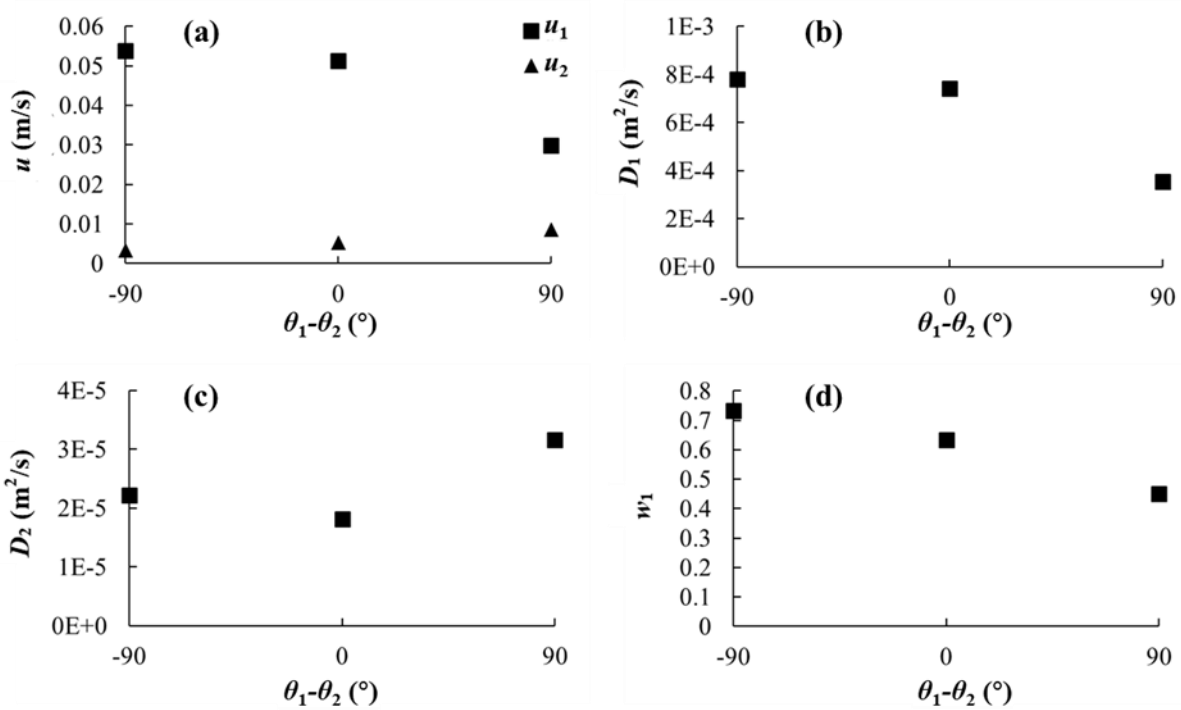

Figure 8. Variation of fitted parameter values with experimental model length for Group 3 experiments. (a) Velocities in the two regions, u_1 and u_2, (b) Dispersion coefficient of region 1, D_1, (c) Dispersion coefficient of region 2, D_2, (d) Water content ratio of region 1, w_1.

Figure 8a shows that as (θ_1 - θ_2) increases from -90° to 90°, u_1 decreases from 5.39×10^{-2} m/s to 2.99×10^{-2} m/s (i.e., by 1.8 times) and u_2 increases from 3.31×10^{-3} m/s to 8.56×10^{-3} m/s (~ 2.6 times). This conforms to the fact that as (θ_1-θ_2) increases, the first peak is delayed and the second peak appears sooner (Fig. 7). The D_1 decreases from 7.81×10^{-4} m^2/s to 3.55×10^{-5} m^2/s (~ 2.2 times) (Fig. 8b); the D_2 increases from 2.22×10^{-5} m^2/s to 3.17×10^{-5} m^2/s (~ 1.4 times) (Fig. 8c). w_1 decreases from 0.732 to 0.451 (~ 1.6 times) while w_2 increases from 0.268 to 0.549 (~ 2 times) (Fig. 8d). The changes in w_1 and w_2 values are consistent with a smaller first peak and a larger second peak (Fig. 7).

This is the preprint of a paper published in Journal of Hydrology Volume 590, November 2020, 125255,
https://doi.org/10.1016/j.jhydrol.2020.125255

3.4 Parameter identifiability

As presented in section 3.1, the variation of the estimated parameter set for the 10-20-30-30 experiment does not show a trend consistent with that of other experiments. We thus perform a study to check the identifiability of model parameters for various Group 1 experiments based on the statistics extracted from respective MCMC chains. The priori distribution of DRAD parameters used in the MCMC calibration of the two experiments is shown in Table 5. Figures 9 and 10 present the MCMC statistics for the 10-20-30-30 and 10-60-30-30 experiments, respectively. The on-diagonal plots of these figures are the estimated posterior parameter distributions for each parameter, while the off-diagonal plots correspond to scatterplots between parameter pairs. A widespread point cloud on the scatterplots indicates that the parameters are independent. A narrow stripe on the scatterplots means a strong correlation between two parameters. The correlation intensity is quantified by the correlation coefficient r (as defined by Eq. 8), which is indicated in the scatterplots. The 95 percentiles of the breakthrough curves are shown in the inset above the diagonal.

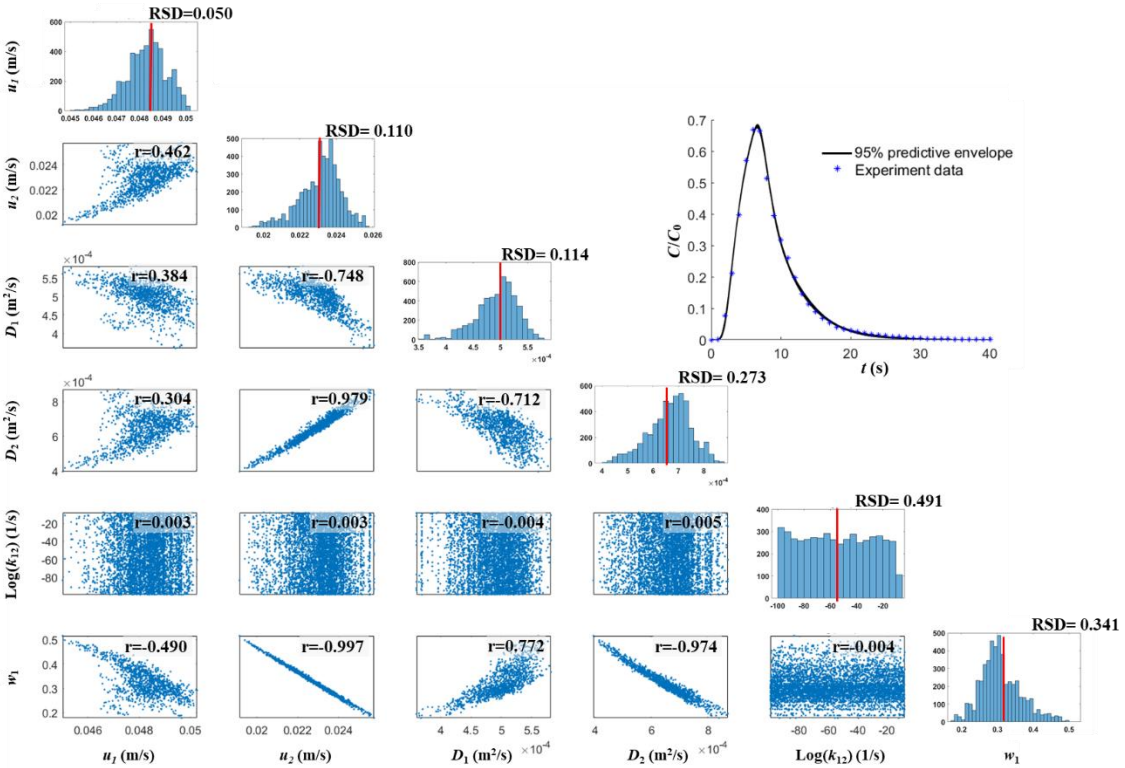

This is the preprint of a paper published in Journal of Hydrology Volume 590, November 2020, 125255,
https://doi.org/10.1016/j.jhydrol.2020.125255

Figure 9. MCMC solutions to the experiment of 10-20-30-30.

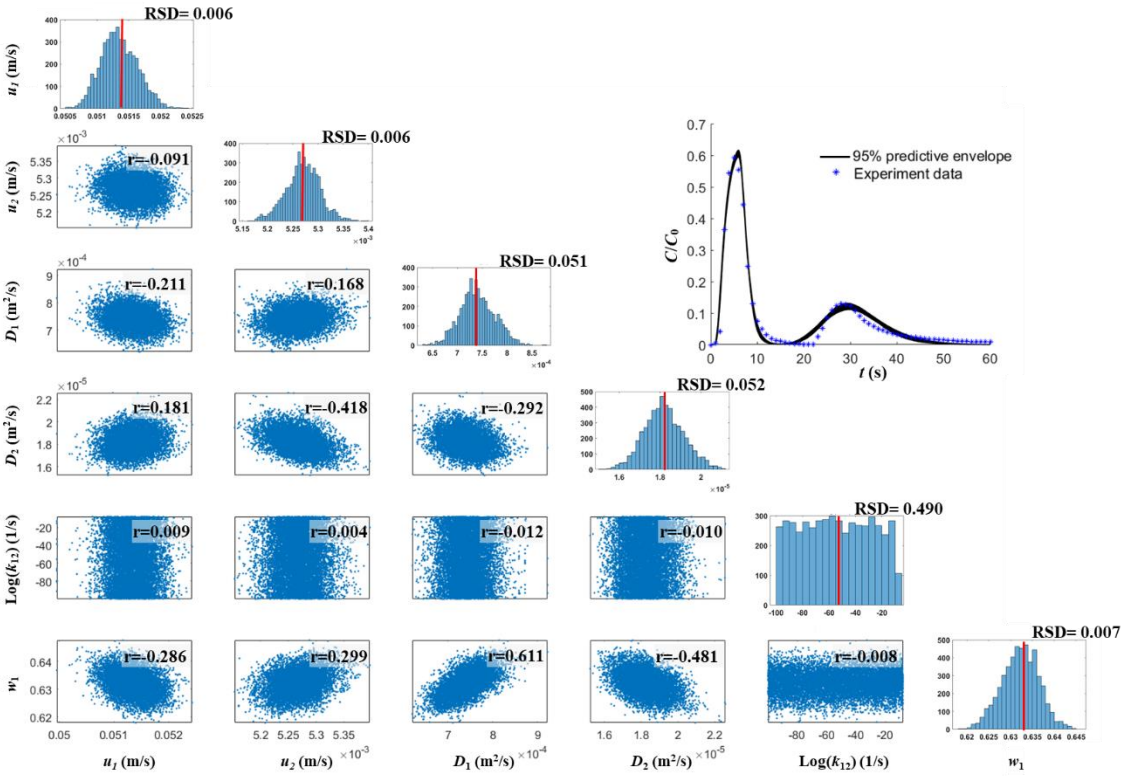

Figure 10. MCMC solutions to the experiment of 10-60-30-30.

Table 5. A priori distribution of DRAD parameters used in the MCMC calibration

	Initial input		Range		Distribution
	10-20-30-30	10-60-30-30	Min	Max	
u_1 (m/s)	3.04×10^{-2}	5.50×10^{-2}	$u_1\times0.005$	$u_1\times200$	Uniform
u_2 (m/s)	1.60×10^{-2}	5.30×10^{-3}	$u_2\times0.005$	$u_2\times200$	Uniform
D_1 (m^2/s)	8.71×10^{-4}	9.30×10^{-4}	0	$500\times D_1$	Uniform
D_2 (m^2/s)	6.00×10^{-6}	1.82×10^{-5}	0	$500\times D_2$	Uniform
k_{12} (1/s)	4.50×10^{-8}	4.50×10^{-8}	1.00×10^{-100}	1.00×10^{-5}	Uniform
w_1 (–)	0.5	0.6325	0.01	0.99	Uniform

It can be seen that except for k_{12}, all other parameters are appropriately identified as their posterior distribution is Gaussian (Fig. 9). In a simple sensitivity test, we observe that varying k_{12} within a wide range between 10^{-90} and

10^{-8} and fixing all other parameters, there is no change in the outlet breakthrough curve. Changes in breakthrough curves only occur when k_{12} takes a large value, which is on the magnitude of 10^{-3}. This means that the model is insensitive to k_{12} as long as its value is small.

For the other parameters, the 10-20-30-30 experiment exhibited a strong interaction between parameters (Fig. 9). According to the parameter correlation plots, we find some parameter pairs, for example, u_2-D_2, u_2-w_1 and D_2-w_1, even exhibited a linear trend on the cross plot. The strong correlations are also shown by the high values of correlation coefficients $|r|$ (nearly equal to 1; Fig. 9). The other parameter pairs like u_2-D_1, D_1-D_2 and D_1-w_1 exhibited a slightly lower correlation strength, with $|r|$ values of 0.748, 0.712 and 0.772.

In contrast, the 10-60-30-30 experiment exhibited stronger parameter identifiability and much weaker parameter interaction (Fig. 10). No obvious correlation between the parameters was found. The maximum $|r|$ value of 0.611 was found for the parameter pair D_1-w_1. The variation range of posterior distributions of the parameters was also smaller. The dispersion coefficients, D_1 and D_2, have the largest RSD values of 0.051 and 0.052, respectively. The RSD values of other parameters such as u_1, u_2, w_1 are quite small, i.e., 0.006, 0.006, 0.007, respectively. These observations indicate the DRAD model parameters were properly identified for the 10-60-30-30 experiment. Similar behavior has also been found for other experiments (not shown here) with larger conduit length ratios.

This is the preprint of a paper published in Journal of Hydrology Volume 590, November 2020, 125255,
https://doi.org/10.1016/j.jhydrol.2020.125255

4. Discussion

4.1 Representativeness of the experiments for karst tracer tests

We examine to which degree our experiments are representative of natural karst systems and the possibility to extrapolate our laboratory finding to the characterization of karst aquifers based on field tracer tests. We calculate three dimensionless quantities (i.e., the conduit length to diameter ratio, Péclet number and Reynolds number) to evaluate the geometric, kinematic and dynamic similarities between our experiments and previous field studies (Table 6, see also Appendix A for a summary of parameter values reported in the literature). The Péclet number Pé is a measure of the relative importance of advection versus diffusion. It is defined as:

$$\text{Pé} = \frac{Lu}{D}, \tag{10}$$

where L is the characteristic length (L), u is the local flow velocity (LT^{-1}), D is the diffusion coefficient (L^2T^{-1}). The Reynolds number Re is the ratio of inertial forces to viscous forces within a fluid:

$$\text{Re} = \frac{\rho u d}{\mu}, \tag{11}$$

where ρ is the density of the fluid (ML^{-3}), u is the local flow velocity (LT^{-1}), d is the diameter of the tube (L), μ is the dynamic viscosity of the fluid ($ML^{-1}T^{-1}$).

The range of values of the geometric and kinematic similarity criteria (i.e., the conduit length-diameter ratio and Péclet number) of our experiments fall within the range of values obtained under field conditions. Regarding the dynamic similarity criterion, the Reynolds number of our experiments is quite small compared to that obtained from field tracer tests. In our experiments, the fluid flow in conduits is laminar (i.e., Re < 2000), while it is well known that the turbulent flow often occurs in natural karst aquifers. Although the difference in flow regime may induce a discrepancy in pressure or flow rate in the conduits, the general trend that the flow rate is positively correlated to the hydraulic head gradient is still respected. Thus, the observed effect of conduit geometry on transport responses may still provide important insights for the interpretation of field tracer tests in natural karst systems.

279 **Table 6.** Comparison of dimensionless quantities between published field data and our experiments

Similarity criterion	Dimensionless number		Range of Values in nature (karst tracer tests)	Range of Values for the experiment
Geometry	Conduit length to diameter ratio	$\frac{l}{d}$	25-25000	37.5-162.5
Kinematic	Péclet number	$\frac{Lu}{D}$	12-331	7.77-21.27
Dynamic	Reynolds number	$\frac{\rho u d}{\mu}$	6500-87000	144

280 Our experimental work confirms that the dual conduit structure generally results in dual-peaked BTCs, as
281 shown in previous studies (Smart, 1988; Perrin and Luetscher, 2008; Field and Leij, 2012). We further found that the
282 number of peaks in the BTCs is not necessarily the same as the number of conduits when the length of the two
283 conduits is similar. For example, the BTC of experiment 10-20-30-30 showed only one peak. The single peak is
284 composed of two overlapping concentration fronts, whose arrival times to the outlet are similar.

285 **4.2 Inferring conduit lengths from dual-peaked BTCs**

286 We propose to use tracer BTCs to infer the length of conduits that form a looped network as shown in Figure 1
287 and Figure B1. For dual-peaked BTCs, we denote the areas below the first and second peaks by A_1 and A_2 respectively.
288 For cases where the two peaks are fully separated, A_1/A_2 may be used to approximate the ratio of the tracer amount
289 of the two conduits. When the Péclet number is sufficiently high (as in our experiments, Pé ranges from 7.77 to
290 21.27), advection dominates the flow process. The flow rate ratio between the conduits may thus be approximated
291 with the ratio of tracer amount passing through the two conduits, i.e., $Q_1/Q_2 \approx A_1/A_2$ (see Appendix B for details). The
292 mean travel times of the two packs of tracer at the outlet may be estimated by the concentration peak times t_{peak1} and
293 t_{peak2}. If all conduits are assumed to have a constant diameter, that may be estimated by field investigations, by

applying mass conservation at the diverging and converging points of the dual-conduit network, the length of the shorter and longer conduits can be estimated by:

$$l_{1e} = \frac{Q_1\left[\left(Q_1+Q_2\right)t_{\text{peak}1} - LS_{\text{f}}\pi R^2\right]}{Q_2\pi R^2}, \tag{12}$$

$$l_{2e} = \frac{Q_2 t_{\text{peak}2} + Q_1 t_{\text{peak}1} - LS_{\text{f}}\pi R^2}{\pi R^2}, \tag{13}$$

where l_{1e} and l_{2e}, are respectively the estimated lengths of the shorter and longer conduits; L is the total length of the dual-conduit structure, i.e., the distance from the injection point to the sampling point via the shorter conduit, S_f is the sinuosity factor, R is the conduit radius, Q_1 and Q_2 are respectively the flow rates of shorter and longer conduits.

We validate the proposed method for estimating lengths of subsurface conduits by applying it to our experimental data of Groups 1 and 2. The ratios between the estimated length and the actual length for the two conduits, $l_{1e}/\ l_1$ and $l_{2e}/\ l_2$ are shown in Figure 11. It can be seen that the length ratios for various experiments scatter around 1.0, which indicates an effective estimation. The average value of this ratio is 1.058, the estimated values tend to be slightly larger than the true value. The shorter conduit length seems better identified than that of the longer conduit. This may be caused by the stronger skewness of the second peak (i.e., stronger dispersion in the longer conduit). The most biased case is the 10-60-30-120 experiment, where the ratio for the shorter conduit, $l_{1e}/\ l_1 = 1.20$. However, the ratio is still very close to 1.0. This indicates that the proposed method is valid at least for the tested conduit network configurations and flow conditions. It is stressed that the method is based on the assumption the conduit diameter is constant for the entire system and is known. The geometrical complexity of natural karst system may invalidate the assumption and imply considering an equivalent conduit diameter. Obviously, the method should be checked for the more general cases of variable conduit diameter when experimental data for such experiments become available.

The method is applicable when BTCs show fully separated dual peaks. Its usage may be hindered if the two

peaks overlap each other. For instance, in the interpretation of the BTCs of the 10-40-30-30 and 10-60-120-30 experiments, we used the local minimum concentration point between the two peaks to approximately separate them and assess the areas under the two peaks. The results of estimated conduit lengths appear reasonably good. On the other hand, the method is expected to be inaccurate when the two peaks are further separated. For example, in Experiment 60-360-30-30, the small value of the second peak makes it difficult to evaluate A_2 because the concentration value is of the same order of magnitude as the background noise signal. For real karst tracer tests, the low concentration signal is very possible to be hidden behind the background noise signals. This suggests us not to ignore the low concentration signals when performing tracer tests in real karst aquifers. Because this low concentration peak may indicate the existence of very long secondary conduits, through which a few quantities of tracer is transported.

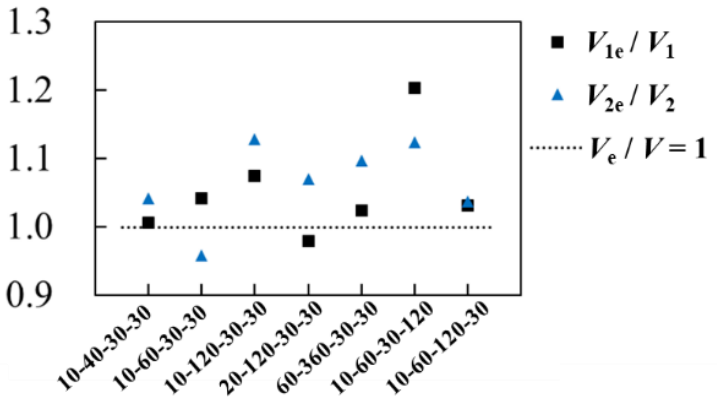

Figure 11. Calculated values of estimated to true conduit length ratio for various experiments.

4.3 Parameter identifiability of DRAD model

The distributions for the sets of parameters of 10-20-30-30 exhibited a strong interaction (u_2-D_1, D_1-D_2, D_1-w_1). In the 10-20-30-30 experiment, the concentration fronts from the two flowing regions do not separate, i.e., the concentration is similar at a certain time. On the other hand, solute migration in the two regions of DRAD is modeled using two similar transport equations. Since the two transport equations have to handle similar concentration, it is

likely that the contribution of the two transport equations to the model responses is indistinguishable. However, it should be noted that the issue of difficult to separate model parameters observed in our study is different from the equifinality issue as discussed in Younes et al., (2016). Younes et al (2016) used a similar dual flowing continuum model to examine transport problems in porous media that includes biofilm phases. The equifinality of their model due to the non-separated concentration fronts in model responses results essentially from a high exchange rate between the dual flowing phases. In contrast, in our experiments there is almost no mass exchange between the two regions. The non-separation of concentration peaks results from the similar arrival times of two packs of solute travel through the two conduits.

According to the RSD and *r* values, the fitting MCMC chain of 10-60-30-30 showed weaker interaction. The DRAD showed different parameter identifiability for 10-20-30-30 and 10-60-30-30 data. One model may perform good parameter identifiability when characterizing a given BTC and exhibits weak identifiability for another one. This has been noted by previous studies (Wagner and Harvey, 1997; Kelleher et al., 2013; Rana et al., 2019). It seems necessary to study the model parameter identifiability with more cases.

For the single-peaked BTC, the DRAD model may reproduce the curve sufficiently well but some of the estimated parameters show strong correlations. This indicates that the DRAD is not optimally parsimonious for single-peaked BTC. For the dual-peaked BTCs, DRAD can adequately characterize the dual-peaked BTCs on the whole with good parameter identifiability, but does not characterize the skewness of the BTC peaks satisfactorily. Finding an optimal model for all situations is beyond the scope of the present study and is left for future research.

Model fitting yields a negligible exchange rate k_{12}. This is attributed to the difference between the conceptual structure of the DRAD model and the physics of the transport process in the experiment. In the DRAD model, mass exchange is assumed to take place along the entire model length, while in the experimental setup mass exchange only occurs at the divergence and convergence between the two conduits.

This is the preprint of a paper published in Journal of Hydrology Volume 590, November 2020, 125255,
https://doi.org/10.1016/j.jhydrol.2020.125255

5. Conclusion

In this paper, we studied the solute transport process in dual conduit structures by lab-scale experiments. The main contributions of this study are summarized as follows.

First, we studied how the dual-conduit structure may influence the BTCs shape, specifically: 1) As the length ratio increases, on the *C*-PV plot, the two peaks get more separated, the concentration value of the first peak (C_{peak1}) increases and the second peak (C_{peak2}) decreases; 2) As the total length increases, the two peaks become increasingly separated and the concentration value of both peaks decreases, while C_{peak2} decreases much more than C_{peak1}; 3) As the (θ_1-θ_2) value of the dual-conduit connection increases, the size of the first peak (A_1), and thus the mass transported through the shorter conduit, gets smaller and the size of the second peak (A_2), and thus the mass transported through the longer conduit, gets bigger.

Second, we proposed a method to estimate underground conduit length from recorded dual-peaked BTCs, assuming a known average conduit diameter. The method exhibits good performance when applied to the experimental BTCs. Whether the method applies to the interpretation of real karst tracer tests needs to be further confirmed by fully controlled field experiments.

Third, we studied the ability of the DRAD model to reproduce BTCs with a single peak and double peaks. For the single-peaked BTCs, the experimental data are well reproduced, but the low parameter identifiability indicates that the DRAD model is non-optimally parsimonious. For dual-peaked BTCs, the DRAD model achieves a good fitting with stronger parameter identifiability, although the exchange coefficient is consistently negligible. For some experiments, the model fails to reproduce the skewness of some parts of the slower peaks. While it may be considered useful for predictive purposes for a given site on which it has been properly calibrated, the analysis of the fitting results shows that its parameters do not necessarily bear a physical meaning. A path for research thus focuses on the development of models, the parameters of which would reflect the geometric and hydraulic reality of the experiments.

This is the preprint of a paper published in Journal of Hydrology Volume 590, November 2020, 125255,
https://doi.org/10.1016/j.jhydrol.2020.125255

376 The following limitations are acknowledged for the present study: (i) the flow regime in the experiments is
377 laminar, while it can be turbulent in field tracer tests, (ii) structures with variable conduit diameter were not studied,
378 (iii) neither the influence of varying flow velocities. Studying the influence of such factors is the subject of ongoing
379 research.

Acknowledgments

C. W. is supported by the China Scholarship Council (CSC) from the Ministry of Education of P.R. China. X.W. and H. J. are grateful for financial support from the European Commission through the Partnership for Research and Innovation in the Mediterranean Area (PRIMA) program under Horizon 2020 (KARMA project, grant agreement number 01DH19022A).

Reference

Berkowitz, B., Cortis, A., Dentz, M. and Scher, H., 2006. Modeling non-Fickian transport in geological formations as a continuous time random walk. Reviews of Geophysics, 44(2).

Dewaide, L., Collon, P., Poulain, A., Rochez, G. and Hallet, V., 2018. Double-peaked breakthrough curves as a consequence of solute transport through underground lakes: a case study of the Furfooz karst system, Belgium. Hydrogeology journal, 26(2), pp.641-650.

Doummar, J., Margane, A., Geyer, T. and Sauter, M., 2012. Artificial Tracer Test 5A – June 2011. - Special Report No. 6 of Technical Cooperation Project "Protection of Jeita Spring", Department of Applied Geology, University of Göttingen, Germany & Federal Institute for Geosciences and Natural Resources (BGR), Germany.

Duran, L., Fournier, M., Massei, N. and Dupont, J.P., 2016. Assessing the nonlinearity of karst response function under variable boundary conditions. Groundwater, 54(1), pp.46-54.

Field, M.S., 1999. The QTRACER program for tracer-breakthrough curve analysis for karst and fractured-rock aquifers (Vol. 98). National Center for Environmental Assessment--Washington Office, Office of Research and Development, US Environmental Protection Agency.

Field, M.S., 2002. The QTRACER2 program for tracer-breakthrough curve analysis for tracer tests in karstic aquifers and other hydrologic systems. National Center for Environmental Assessment--Washington Office, Office of Research and Development, US Environmental Protection Agency.

Field, M.S. and Leij, F.J., 2012. Solute transport in solution conduits exhibiting multi-peaked breakthrough curves. Journal of Hydrology, 440, pp.26-35.

Florea, L.J. and Wicks, C.M., 2001. Solute transport through laboratory-scale karstic aquifers. Geography/Geology Faculty Publications, p.11.

406 Goldscheider, N. and Drew, D., 2007. Methods in karst hydrogeology. International Contributions to
407 Hydrogeology, 26.
408 Goldscheider, N., Meiman, J., Pronk, M. and Smart, C., 2008. Tracer tests in karst hydrogeology and speleology.
409 International Journal of Speleology, 37(1), pp.27-40.
410 Göppert, N. and Goldscheider, N., 2008. Solute and colloid transport in karst conduits under low‐ and high‐
411 flow conditions. Groundwater, 46(1), pp.61-68.
412 Goeppert, N., Goldscheider, N. and Berkowitz, B., 2020. Experimental and modeling evidence of kilometer-
413 scale anomalous tracer transport in an alpine karst aquifer, 115755.
414 Haario, H., Laine, M., Mira, A. and Saksman, E., 2006. DRAM: efficient adaptive MCMC. Statistics and
415 Computing, 16(4), pp.339-354.
416 Hauns, M., Jeannin, P.Y. and Atteia, O., 2001. Dispersion, retardation and scale effect in tracer breakthrough
417 curves in karst conduits. Journal of Hydrology, 241(3-4), pp.177-193.
418 Kelleher, C., Wagener, T., McGlynn, B., Ward, A. S., Gooseff, M. N., & Payn, R. A. (2013). Identifiability of
419 transient storage model parameters along a mountain stream. Water Resources Research, 49(9), 5290-5306.
420 Li, G., Loper, D.E. and Kung, R., 2008. Contaminant sequestration in karstic aquifers: Experiments and
421 quantification. Water Resources Research, 44(2).
422 Majdalani, S., Guinot, V., Delenne, C. and Gebran, H., 2018. Modeling solute dispersion in periodic
423 heterogeneous porous media: Model benchmarking against experiment experiments. Journal of Hydrology, 561,
424 pp.427-443.
425 Maloszewski, P., Harum, T. and Benischke, R., 1992. Mathematical modeling of tracer experiments in the karst
426 of Lurbach system. Steierische Beiträge zur Hydrogeologie, 43, pp.116-136.
427 Massei, N., Wang, H.Q., Field, M.S., Dupont, J.P., Bakalowicz, M. and Rodet, J., 2006. Interpreting tracer
428 breakthrough tailing in a conduit-dominated karstic aquifer. Hydrogeology Journal, 14(6), pp.849-858.
429 Mohammadi, Z., Gharaat, M.J. and Field, M., 2019. The Effect of Hydraulic Gradient and Pattern of Conduit
430 Systems on Tracing Tests: Bench-Scale Modeling. Groundwater, 57(1), pp.110-125.
431 Morales, T., Uriarte, J.A., Olazar, M., Antigüedad, I. and Angulo, B., 2010. Solute transport modelling in karst
432 conduits with slow zones during different hydrologic conditions. Journal of hydrology, 390(3-4), pp.182-189.
433 Moreno, L. and Tsang, C.F., 1991. Multiple-peak response to tracer injection tests in single fractures: A
434 numerical study. Water Resources Research, 27(8), pp.2143-2150.

Perrin, J. and Luetscher, M., 2008. Inference of the structure of karst conduits using quantitative tracer tests and geological information: example of the Swiss Jura. Hydrogeology Journal, 16(5), pp.951-967.

Rana, S. M., Boccelli, D. L., Scott, D. T., & Hester, E. T., 2019. Parameter uncertainty with flow variation of the one-dimensional solute transport model for small streams using Markov chain Monte Carlo. Journal of Hydrology, 575, pp.1145-1154.

Skopp, J., Gardner, W.R. and Tyler, E.J., 1981. Solute movement in structured soils: Two-region model with small interaction. Soil Science Society of America Journal, 45(5), pp.837-842.

Smart, C.C., 1988. Artificial tracer techniques for the determination of the structure of conduit aquifers. Groundwater, 26(4), pp.445-453.

Upchurch, S., Scott, T.M., ALFIERI, M., Fratesi, B. and Dobecki, T.L., 2018. The Karst Systems of Florida: Understanding Karst in a Geologically Young Terrain. Springer.

Van Genuchten, M.T. and Wierenga, P.J., 1976. Mass transfer studies in sorbing porous media I. Analytical solutions 1. Soil Science Society of America Journal, 40(4), pp.473-480.

Vrugt, J.A., Clark, M.P., Diks, C.G., Duan, Q. and Robinson, B.A., 2006. Multi-objective calibration of forecast ensembles using Bayesian model averaging. Geophysical Research Letters, 33(19).

Wagner, B.J. and Harvey, J.W., 1997. Experimental design for estimating parameters of rate−limited mass transfer: Analysis of stream tracer studies. Water Resources Research, 33(7), pp.1731-1741.

Younes, A., Delay, F., Fajraoui, N., Fahs, M. and Mara, T.A., 2016. Global sensitivity analysis and Bayesian parameter inference for solute transport in porous media colonized by biofilms. Journal of Contaminant Hydrology, 191, pp.1-18.

Zhao, X., Chang, Y., Wu, J. and Peng, F., 2017. Laboratory investigation and simulation of breakthrough curves in karst conduits with pools. Hydrogeology Journal, 25(8), pp.2235-2250.

Zhao, X., Chang, Y., Wu, J. and Xue, X., 2019. Effects of flow rate variation on solute transport in a karst conduit with a pool. Environmental Earth Sciences, 78(7), pp.237.

This is the preprint of a paper published in Journal of Hydrology Volume 590, November 2020, 125255,
https://doi.org/10.1016/j.jhydrol.2020.125255

Appendix A.

The diameter of karst conduit ranges from a few centimeters to several meters (Upchurch et al., 2018). The karst aquifer length is between 0.5 km to 10 km (Morales et al., 2010; Göppert and Goldscheider, 2008; Duran et al., 2016). Various flow velocities have been reported: 31.9 ~ 117.6 m/h (Morales et al., 2010), 24.8 ~ 136.9 m/h (Göppert and Goldscheider, 2008) and 63 ~ 121.4 m/h (Duran et al., 2016). If we assume the water viscosity μ = 1 mPa·s and the lower and upper values for conduit diameter are 0.2 m and 2 m, the Reynolds numbers are approximately 6500 ~ 44000 (Morales et al., 2010), 7600 ~ 34000 (Göppert and Goldscheider, 2008), 6700 ~ 87000 (Duran et al., 2016), respectively. This indicates that the natural karst flow is frequently under turbulent flow regime. In our experiments, the inlet flow velocity v = 0.054 m/s and conduit diameter d = 0.004 m. Thus, the characteristic Reynolds number Re = 144, i.e. the experiments are under the laminar flow condition. For real karst systems in previous studies, the calculated Peclet number range is 167 ~ 256 (Massei et al., 2006), 77 ~ 140 (Field, 1999), 12 ~ 113 (Field, 2002), 279 ~ 331 (Doummar et al., 2012). The Peclet number of our experiments lies between 7.77 and 21.27.

Appendix B.

The schematic diagram for natural karst systems with a dual conduit structure is shown in Figure B1. l' and l'' are the lengths of the two convergence conduit parts, Q_0 is the flow rate of these two parts, l_1 and l_2 are the lengths of the shorter and the longer conduit, Q_1 and Q_2 are the flow rates of the shorter and the longer conduit. From the mass conservation law, we have:

$$Q_0 = Q_1 + Q_2 . \tag{B1}$$

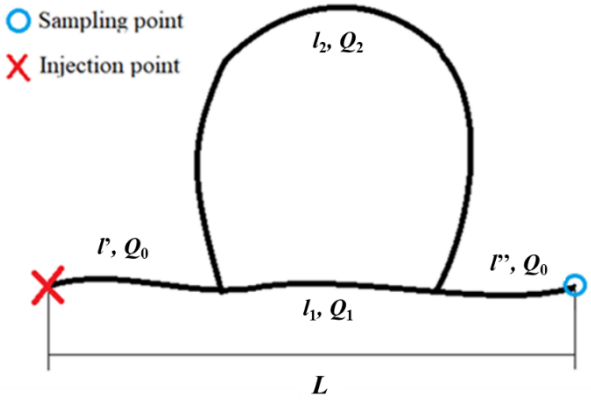

478

479 **Figure B1.** Schematic diagram of a dual-conduit structure.

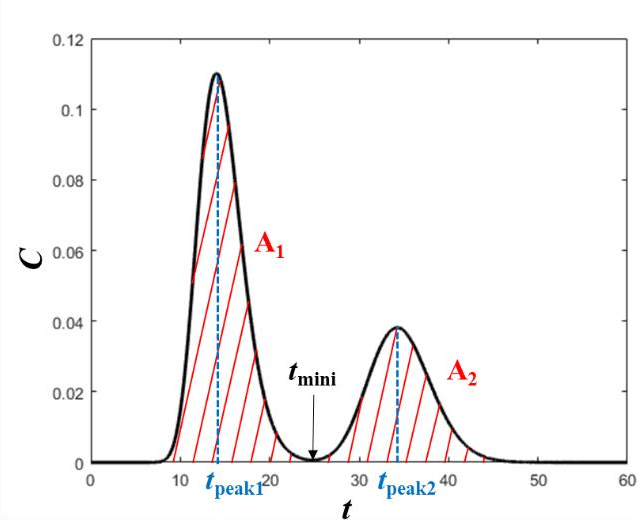

480

481 **Figure B2.** Definition sketch for conduit length estimation using BTCs.

482 Figure B2 presents a typical double-peaked BTC resulted from a dual-conduit structure shown in Figure B1.

483 When the two peaks are fully separated, the tracer mass that migrated through the two conduits can be calculated by:

484 $$m_1 = \int_{t=0}^{t_{mini}} Q_0 C(t) dt = Q_0 \int_{t=0}^{t_{mini}} C(t) dt = Q_0 A_1 , \quad \text{(B2)}$$

485 $$m_2 = \int_{t_{mini}}^{t_{max}} Q_0 C(t) dt = Q_0 \int_{t_{mini}}^{t_{max}} C(t) dt = Q_0 A_2 , \quad \text{(B3)}$$

486 where t_{mini} is the time when the concentration reaches the minimum value between the two peaks, t_{max} is the final

487 time of the tracer test, Q_0 is the flow rate at the outlet point, C(t) is the transient concentration at the outlet point; A_1

488 is the area below the first peak of the BTC, A_2 is the area below the second peak.

From Equations B2 and B3, we have:

$$\frac{m_1}{m_2} = \frac{A_1}{A_2}. \tag{B4}$$

Assuming that advection dominates the transport process, the tracer mass that enters the two conduits can also be approximated at the upstream connector where the flow and mass are diverged (Figure B3) by:

$$m_1 \approx \int_{t=0}^{t_{max}} Q_1 C(t)dt = Q_1 \int_{t=0}^{t_{max}} C(t)dt, \tag{B5}$$

$$m_2 \approx \int_{t=0}^{t_{max}} Q_2 C(t)dt = Q_2 \int_{t=0}^{t_{max}} C(t)dt. \tag{B6}$$

Therefore

$$\frac{m_1}{m_2} = \frac{A_1}{A_2} \approx \frac{Q_1}{Q_2}, \tag{B7}$$

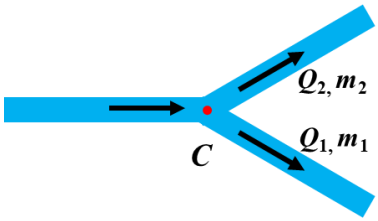

Figure B3. Schematic diagram showing the division of flow and mass into the two conduits at the connector.

From Equations (B1) and (B7), the flow rates in the two conduits, Q_1 and Q_2, can be estimated. The total length of the system L is evaluated from:

$$L \times S_f = l' + l_1 + l'' = \frac{V' + V_1 + V''}{\pi R^2} = \frac{V_0 + V_1}{\pi R^2} \tag{B8}$$

where L is the distance between the inlet and the outlet points; S_f is the sinuosity factor to estimate underground conduit length; V', V'', V_1 are respectively the volumes of the inlet, outlet, and shorter conduits, l', l'', l_1 are the corresponding conduit lengths, V_0 is the sum of V' and V''.

The concentration peak times t_{peak1} and t_{peak2} may represent the mean tracer travel time, thus,

$$\frac{V_0}{Q_1 + Q_2} + \frac{V_1}{Q_1} = t_{peak1}, \tag{B9}$$

$$\frac{V_0}{Q_1 + Q_2} + \frac{V_2}{Q_2} = t_{peak2}, \tag{B10}$$

where V_2 is the volume of the longer conduit. In Equations B8 to B10, the value of L, S_f, Q_1, Q_2, t_{peak1} and t_{peak2} may be estimated from field surveys. Thus, the three unknown variables V_1, V_2 and V_0 can be obtained by solving Equations B8 to B10 together:

$$V_1 = \frac{Q_1\left[(Q_1+Q_2)t_{peak1} - LS_f\pi R^2\right]}{Q_2}, \tag{B11}$$

$$V_2 = Q_2 t_{peak2} + Q_1 t_{peak1} - LS_f\pi R^2, \tag{B12}$$

$$V_0 = \frac{(Q_1+Q_2)\left(LS_f\pi R^2 - Q_1 t_{peak1}\right)}{Q_2}. \tag{B13}$$

If the average diameters of the conduits can also be inferred from cave explorations, the lengths of the conduit can thus be obtained by:

$$l_{1e} = \frac{Q_1\left[(Q_1+Q_2)t_{peak1} - LS_f\pi R^2\right]}{Q_2\pi R^2}, \tag{B14}$$

$$l_{2e} = \frac{Q_2 t_{peak2} + Q_1 t_{peak1} - LS_f\pi R^2}{\pi R^2}, \tag{B15}$$

$$l_{0e} = l_e' + l_e'' = \frac{(Q_1+Q_2)\left(LS_f\pi R^2 - Q_1 t_{peak1}\right)}{Q_2\pi R^2}. \tag{B16}$$

Applying this method, we calculate the conduit lengths of our first two groups of experiments according to the BTCs we obtained. Because the 10-20-30-30 experiment BTC has only one peak, the method is not applicable. The calculation process and results are shown in Table B1.

This is the preprint of a paper published in Journal of Hydrology Volume 590, November 2020, 125255,
https://doi.org/10.1016/j.jhydrol.2020.125255

522 **Table B1.** True and estimated values of conduit properties for various dual-conduit systems

Experiment name	10-20 -30-30	10-40 -30-30	10-60 -30-30	10-120 -30-30	20-120 -30-30	60-360 -30-30
True V_1/ (cm^3)	1.27	1.27	1.27	1.27	2.53	7.55
True V_2/ (cm^3)	2.53	5.04	7.55	15.09	15.09	45.25
True l_1/ (cm)	10	10	10	10	20	60
True l_2/ (cm)	20	40	60	120	120	360
Estimated V_1/ (cm^3)	N.A.	1.28	1.32	1.36	2.47	7.73
Estimated V_2/ (cm^3)	N.A.	5.25	7.24	17.04	16.16	49.63
Estimated l_1/ (cm)	N.A.	10.16	10.52	10.86	19.68	61.55
Estimated l_2/ (cm)	N.A.	41.80	57.64	135.63	128.62	394.93